RESEARCH ARTICLE

Micro-viscoelastic Characterization of Compressed Oral Solid Dosage Forms with Ultrasonic Wave Dispersion Analysis

Tipu Sultan[1] · Shubhajit Paul[2] · Enamul Hasan Rozin[1] · Yin-Chao Tseng[2] · Michael C. F. Bazzocchi[1] · Cetin Cetinkaya[1]

Abstract

Due to their constituent powders, the materials of advanced compressed oral solid dosage (OSD) forms are micro-composites and strongly visco-elastic at macro- and micro-length scales. The disintegration, drug release, and mechanical strength of OSD forms depend on its micro-texture (such as porosity) and micro-scale physical/mechanical properties. In the current work, an algorithmic ultrasonic characterization framework for extracting the micro-visco-elastic properties of OSD materials is presented, and its applicability is demonstrated with a model material. The proposed approach is based on the effect of visco-elasticity and granularity on the frequency-dependent attenuation of an ultrasonic wave pulse in a composite (granular) and viscous medium. In modeling the material, a two-parameter Zener model for visco-elasticity and a scattering attenuation mechanism based on Rayleigh scattering for long-wave approximation are employed. A novel linear technique for de-coupling the effects of micro-visco-elasticity and scattering on attenuation and dispersion is developed and demonstrated. The apparent Young's modulus, stress, and strain relaxation time constants of the medium at micro-scale are extracted and reported. Based on this modeling and analysis framework, a set of computational algorithms has been developed and demonstrated with experimental data, and its practical utility in pharmaceutical manufacturing and real-time release testing of tablets is discussed.

Keywords compressed oral solid dosage forms · micro-structure · micro-visco-elasticity · non-destructive characterization · particulate composites · physical properties · porosity · ultrasonic wave dispersion

Introduction

A modern compressed oral solid dosage (OSD) form (pharmaceutical tablet) is a consumable drug delivery device with fine-tuned properties. The dissolution profile, release mechanisms, and active materials release rate of an OSD form depend on its various physical/mechanical and microstructure/morphological properties, such as its tensile strength, porosity, internal pore- and microstructure, inter-granular coupling, and visco-elastic properties [1–3].

Pharmaceutical development and production benefit from the use of non-destructive methods for precise and rapid micro-scale material characterization and efficient monitoring for related meso-scale parameters (e.g., tensile strength, visco-elasticity, and porosity), related to critical quality attributes (CQA). Because of its non-destructiveness, the potential for real-time *in situ* quality monitoring, and comparatively inexpensive equipment and operational costs, the direct approach of obtaining material characteristics from the transmission and dispersion of propagating elastic waves in its medium is appealing. Consequently, elastic wave techniques (both acoustic and ultrasonic) have been employed to characterize pharmaceutical compressed OSD forms such as tensile strength of compacts [4], material particle size and porosity [5], acoustic emission while compaction of the OSD [6], the integrity of tablets and elasticity [7–12], elastic property measurements of multi-layer tablets [13], the effect of shape on the physical–mechanical properties of the pharmaceutical tablet [14], and complete anisotropic

✉ Cetin Cetinkaya
  ccetinka@clarkson.edu

1   Department of Mechanical and Aerospace Engineering Photo-Acoustics Research Laboratory, Clarkson University, Potsdam, New York 13699-5725, USA

2   Material and Analytical Sciences, Boehringer Ingelheim Pharmaceuticals, Inc. Ridgefield, Ridgefield, Connecticut 06877, USA

🌀 **aaps**

🙾 Springer

characterization of OSD forms [15]. It is also shown that ultrasonic waves are sensitive to micro/macro-cracks and other defects [16, 17], capping risk [18, 19], mechanical strength ("hardness") [20], and production process parameters such as the compaction speed, compaction pressure, and head flat types [21].

Typically, the powder materials used in advanced OSD forms are highly visco-elastic and granular (composite), so a practical characterization technique must be capable of dealing with both effects simultaneously. In this study, the characterization of the visco-elastic properties of pharmaceutical granular materials is conducted while taking scattering effects into account for the first time. Visco-elasticity is linked to temporal responses of a compact such as creep, damping, and stress relaxations in its material. Common excipients used in modern pharmaceutical manufacturing are organic/polymeric with strong visco-elastic/visco-plastic properties [22]. Such properties play critical roles in a solid dosage design since tablets are plastically shaped by a high-strain rate compaction force involving the intrinsic properties of active pharmaceutical ingredient(s) (API) and excipients from powder form to solid state, followed by relatively long relaxation times as some other production unit operations (such as coating, packaging, handling, storage, and transport) take place. Mechanical relaxation is related to visco-elasticity, leading to stored strain energy during compaction, pore and crack formation and propagation, and grain separation at micro-scale in a tablet matrix.

Elastic wave pulses traveling in a solid medium are affected by the visco-elasticity of its constituents and geometric discontinuities and defects such as micro-structure/textures, inter-granular boundaries with air gaps (i.e., porosity), and micro/macro-cracks (e.g., scattering and wave localization effects). Thus, the spectral content and amplitude of a traveling elastic wave packet are modulated as it travels in a spatially textured (composite) medium when wavelengths are sufficiently short compared to the characteristic length scale of the media texture. Thus, the attenuation of the wave pulse includes information on the dissipation mechanisms (i.e., visco-elasticity and internal friction) of the medium and the nature of its wave scatters (such as particle/grain/pore size distribution, grain-matrix boundaries, micro-cracks, voids, inclusions, macro-cracks (e.g., pre-capping shear planes), and other structural defects and irregularities (such as non-uniforms mass density distributions of APIs).

Scattering attenuation for metals with no or weak visco-elasticity has been studied since the 1950s by considering the grain-matrix elasticity and coupling, dimensions and forms of the geometry characteristics, and the leading wavelength of the propagating wave pulse [23]. The standard linear solid (Zener) model is often used as an acceptable approximation for modeling visco-elasticity of polymeric materials according to various studies [24, 25]. However, in a granular medium, the observed complete attenuation is more dominant than in the single crystal medium of the same material (assuming that the visco-elastic constants remain unchanged) due to wave scattering. Accordingly, to precisely characterize the visco-elastic properties and extract the microstructure of the OSD medium, scattering must be understood and considered in a mathematical modeling effort. When an ultrasonic pulse propagates through a polycrystalline material, its elastic and mass density characteristics as well as inhomogeneities and discontinuities (e.g., cracks) lead to the difference in propagation speeds of each crystallite, consequently causing wavefront coherency loss and scattering of the traveling pulse. For correlating measured attenuation to grain size, the following two modeling studies are considered foundational. The first material model by Stanke and Kino [26] depends on a second-order perturbation model [27] to illustrate a unified framework. This model is applicable and valid across all the frequency regions for a cubic equiaxial un-textured polycrystalline medium when the nonlinear equation of the propagating wave constant was acquired. The Stanke-Kino model reproduces the attenuation in the Rayleigh and stochastic regimes [28, 29]. The second material model, known as Weaver's model, [30] provides a general solution utilizing the Dyson and Bethe–Salpeter equation for the untextured cubic-symmetry polycrystals. By applying the Born approximation [31], these two basic models produce the same attenuation coefficient solution and are further extended to some special cases [32, 33]. For instance, Weaver's model was utilized to derive explicit formulas for the ultrasonic wave attenuation coefficients in polycrystals with hexagonal symmetry [34].

The matrix materials of advanced compressed OSD forms are micro-composites, visco-elastic, and granular at macro- and micro-length scales, and thus their morphologies deviate from crystalline solid materials. These visco-elastic properties of the OSDs can be utilized in the development of a reliable predictive tool to assess tablets' robustness and risk of internal or external defects. The key objective of the current study is to provide a deterministic ultrasonic characterization framework for simultaneously extracting the visco-elastic and scattering material parameters of OSD forms from their dispersion relations in a non-destructive manner for the first time. Based on the previously reported observations and experiences [35, 36], in such complex materials, both visco-elastic and scattering mechanisms are expected to be comparably effective in attenuation. To account for the visco-elastic and scattering effects respectively in the OSD material medium at micro-scale, in the current work,

Zener's visco-elastic model is modified and used along with the Rayleigh scattering model. Elastic modulus and stress/strain relaxation time coefficients, as well as Rayleigh scattering parameters, are extracted and reported utilizing the proposed mathematical framework and a novel robotic experimental rig for repeatable waveform acquisition. The use cases of the algorithmic approach in pharmaceutical development, manufacturing, and real-time release testing of tablets are also discussed.

Mathematical Formulation for the Analysis of Attenuation Mechanisms in Effect

As an elastic wave pulse travels in a dissipative field with high granularity, many dispersion mechanisms could affect and modulate its frequency and amplitude over time and space. The total attenuation in a medium is due to energy dissipative (e.g., micro-visco-elasticity, damping, and internal friction) and geometric properties (e.g., reflection and diffraction by grain boundaries, inclusions, voids, micro-cracks, macro-cracks, and other structural irregularities and defects) of the medium material. A mathematical model connecting these properties of elastic wave attenuation and dispersion is required to describe and characterize modern OSD materials for such mechanisms.

In a linear elastic medium, a one-dimensional transient displacement $u(x,t)$ in the x-direction can be depicted in the Fourier integral form:

$$u(x,t) = \int_{-\infty}^{+\infty} G(\omega)\exp(i(\kappa(\omega)x - \omega t))d\omega \quad (1)$$

where t is time, ω the angular frequency, $G(\omega)$, the displacement waveform $u(x, t)$ in the spectral domain (ω) at a reference plane ($x=0$), and $\kappa(\omega) = \beta(\omega) + i\alpha(\omega)$ the dispersion relation (complex wavenumber, $i\sqrt{-1}$) with $\alpha(\omega)$ and $\beta(\omega)$ the attenuation and real (angular) wavenumber, respectively. From Eq. 1, the displacement waveforms at two arbitrary locations $x=0$ and $x=h$ are expressed as:

$$u(x = 0, t) = \int_{-\infty}^{+\infty} G(\omega)\exp(i\omega t)d\omega$$
$$u(x = h, t) = \int_{-\infty}^{+\infty} G(\omega)\exp(i(\kappa(\omega)h - \omega t))d\omega \quad (2)$$

where, in the current context, h represents the thickness of the sample tablet in the propagation direction (x) of the elastic wave pulse represented by its spectral contents $G(\omega)$. In this study, the displacement waveforms $u(x = 0, t)$ and $u(x = h, t)$ are experimentally acquired using ultrasonic equipment. The Fourier transforms (F) of these two waveforms (Eq. 2) yield the following expressions:

$$F\{u(x = 0, t)\} = \sqrt{2\pi}G(\omega) \quad F\{u(x = h, t)\} = \sqrt{2\pi}G(\omega)\exp(i\kappa(\omega)h) \quad (3)$$

The complex wavenumber $\kappa(\omega)$ is then extracted from (Eq. 3) as:

$$\kappa(\omega) = \beta(\omega) + i\alpha(\omega) = -i\frac{1}{h}\ln\left(\frac{F\{u(x = h, t)\}}{F\{u(x = 0, t)\}}\right) \quad (4)$$

with the complex wavenumber $\kappa(\omega) = \beta(\omega) + i\alpha(\omega)$, the propagating wave field is represented as:

$$u(x,t) = \int_{-\infty}^{+\infty} G(\omega)e^{-\alpha(\omega)x}e^{i(\beta(\omega)x-\omega t)}d\omega \quad (5)$$

In practice, a Wiener filter [37] is used to eliminate zero division outside the transducer bandwidth in Eq. 4 and associated numerical instability, and the frequency-dependent phase c_p and group c_g speeds of the dispersive medium are determined by: $c_p(\omega) = \omega/\beta(\omega)$ and $c_g(\omega) = d\omega/d\beta(\omega)$.

Scattering Models for Composite Materials with Micro-structures

For the tablet samples utilized in the current study, a medium material model for dissipation and scattering is developed and presented based on the following assumptions: (*i*) the only attenuation mechanisms present in the material are visco-elastic dissipation and elastic scattering, (*ii*) the interactions of these two attenuation mechanisms are de-coupled, (*iii*) for the visco-elastic behavior the standard linear solid model is valid, (*iv*) the Rayleigh scattering model (as a long-wave approximation) governs the scattering attenuation, (*v*) the particle number present in a sample is adequately high, and the granular size distribution is statistical with a probability density function, and (*iv*) scattering energy is low compared to the total strain energy of the incident wave pulse.

Since the 1950s, based on the works for metals with weak visco-elasticity, it has been known that every grain present in an attenuating material provides scattering-related attenuation based on the proportion of the wavelength of the traveling displacement pulse (λ) to the fixed scatterer size (grain size) (d) of the medium, specifically, λ/d [23, 38]. Under the assumptions listed above for the medium material, three main scattering regimes for non-visco-elastic materials have been identified [39] by the ratio of acoustic wavelength (λ) with the mean grain diameter (d). When d is constant, for $\lambda >> 2\pi d$ (*i.e.* $\lambda/d >> 2\pi$), attenuation (Rayleigh scattering of the medium) is denoted in the frequency (f) terms: $\alpha^s(f, d) = c_r d^3 f^4$ where c_r is an unknown material constant. As wavelength becomes shorter (due to increasing frequency), about $\lambda \sim 2\pi d$, wave propagation enters a new zone, called the stochastic regime, and the

attenuation coefficient is presented as $\alpha^s(f,d) = c_s df^2$ where c_s is also an unknown material constant. To our best knowledge, currently, there is no widely used theory for the real part of the dispersion curve, but in principle, it is known an approximate relation can be established using the Kramers–Kronig (K-K) relationship. As discussed in [26], the assumption for the low scattered energy (assumption *vi* above) is inapplicable in the stochastic regime, where several scattering effects are present. The third regime is characterized by a wavelength that is significantly smaller than the characteristic size of the scatter (i.e., $\lambda < < d$, or $\lambda/d < < 1$), referred to as the diffusion regime, frequency independent: $\alpha^s(d) = c_d/d$ where c_d is an unknown material constant. As multiple scattering is dominant in the diffusion regime, Assumption *vi* is invalid for the diffusion regime. In summary, these asymptotes proposed by [40] for the first time are as follows:

$\lambda \simeq 2\pi d \gg d \Rightarrow \alpha^s(f,d) = c_r d^3 f^4 = c_r d^3 \lambda^{-4}$ Rayleigh Regime (Long Wavelength Range)

$\lambda \approx d \Rightarrow \alpha^s(f,d) = c_s d f^2 = c_s d \lambda^{-2}$ Stochastic Regime (Transition Range)

$\lambda \ll \Rightarrow d \Rightarrow \alpha^s(d) = c_d d^{-1}$ Diffusion Regime (Short Wavelength Range)

$$(6)$$

Based on the approximate velocity of the pressure (longitudinal) wave in the medium and the characteristic size of grains, an ultrasonic transducer with wavelengths in millimeter-scale is specified for the current experimental system, to satisfy the Rayleigh scattering approximation ($\lambda/d > > 1$). For the BI_2022_12kN sample material (Tables I and II), $c_L = 1822.86$ m/s, when it is excited at the upper bound of its frequency band, $f_{upper} = 2.6$ MHz, the wavelength of the pressure wave is approximated as $c_L/f = \lambda = 700.76$ μm. Thus $\lambda \sim 2\pi d^*$, leading to $d^* = 700.76/2\pi = 111.53$ μm. For grains smaller than $d^* = 111.53$ μm, in propagation, *Rayleigh* scattering becomes the dominant attenuation mechanism. As depicted in Fig. 1, the grains of the sample set are substantially smaller than this cut-off diameter $d^* = 111.53$ μm, thus *Rayleigh* scattering is a reasonable model for the presented investigation.

In the case of Rayleigh scattering, the mathematical form $\alpha^s(f,d) = c_r d^3 f^4$ represents the attenuation due to scattering for a uniform (constant) granular size distribution of a particulate composite medium. Bearing in mind a grain size distribution of a scatterer (for example, a composite consisting of grains of various sizes) for the feature size d, defined by a probability density function of $q(d)$ with $\int_{d=0}^{\infty} q(d)\mathrm{d}d = 1$, the contributions from all the grains of a solid body in scattering attenuation can be taken into consideration. For example, if we assume that *Gaussian* probability distribution represents $q(d)$ for the granular sample medium, thus:

$$q(d) = \frac{1}{d\sqrt{2\pi\sigma}}\exp\left(-(\log(d/\mu))^2/2\sigma^2\right) \tag{7}$$

where μ is the median of the *Gaussian* probability distribution in the medium and σ its standard deviation, the total scattering attenuation is expressed in frequency (*f*) for a sample consisting of N_o number of granular scatterers in the propagation direction per unit length as [41]:

$$\alpha^s(f) = \left(c_r N_0 \int_0^\infty q(d)d^3\mathrm{d}d\right)f^4 \tag{8}$$

where c_r is a material constant, for this Gaussian distribution, the total scattering attenuation coefficient becomes:

$$\alpha^s(f) = \left(\frac{c_r N_0}{\sqrt{2\pi\sigma}}\int_0^\infty d^3\exp\left(-(d-\mu)^2/2\sigma^2\right)\mathrm{d}d\right)f^4 \tag{9}$$

where μ is the median of the distribution in the medium and σ its standard deviation. The frequency-dependent visco-elastic and scattering attenuation mechanisms are assumed to have decoupled interactions, and the overall attenuation in the transmitting waves is approximated as: $\alpha(\omega) = \alpha^s(\omega) + \alpha^v(\omega)$. The total attenuation $\alpha(\omega)$, and the wavenumber $\beta(\omega)$ considering the K-K relation, are related by:

$$\alpha(\omega) = \frac{\pi}{2}\beta^2(\omega)\frac{d}{d\omega}\left(\frac{\omega}{\beta(\omega)}\right) \tag{10}$$

As discussed in [42], the closer local approximation to the K-K relation introduced an assumption of the identical behavior for the attenuation coefficient $\alpha(\omega)$ remains outside of the measurement bandwidth. Therefore, an extrapolation outside of this bandwidth is required to determine $\beta(\omega)$ from an experimentally obtained total attenuation relation $\alpha(\omega)$. In the experiment, the measurement bandwidth and the bandwidth of the ultrasonic transducer are the same; therefore, to apply the local approximation of the K-K relation, the attenuation behavior is considered as same in the entire frequency domain. This approximation results in deviance from the computationally determined dispersion term $\beta(\omega)$ from the experimentally obtained curve. To achieve a close agreement with the experimentally extracted wavenumber $\beta(\omega)$ with the extracted term $\beta(\omega)$ requires to modify by adding an arbitrary function considering the K-K relation. The modified total wavenumber, containing both the scattering and visco-elastic dispersion terms, is expressed as:

$$\beta(\omega) = \beta^s(\omega) + \beta^s_{\mathrm{mod}}(\omega) = \beta^v(\omega) + \beta^s(\omega) + A(\omega;\omega_{\min}, \omega_{\max}) \tag{11}$$

where $A(\omega;\omega_{\min}, \omega_{\max})$ is a spectral-dependent function, and $\beta^s_{\mathrm{mod}}(\omega)$ the revised scattering wavenumber. $A(\omega;\omega_{\min}, \omega_{\max})$ can be determined by equating the wavenumber calculation to the experimentally acquired dispersion data using Eq. 10. Preferably, $A(\omega;\omega_{\min}, \omega_{\max})$ is a linear function in ω, so that

Table I The Measured Average Compact Thicknesses (h), Compact Diameters (d), Apparent Masses (m_A), and Apparent Mass Densities (ρ_A) with their Standard Deviations (SD)

Sample sub-sets	Compaction force F_c (kN)	Tablet shape		Measured parameters			
				h	d	m_A	ρ_A
				(mm)	(mm)	(g)	(kg/m^3)
BI_2022_02kN	2	Cylindrical (flat)	Avg	3.68	9.04	0.30	1291.25
			SD	0.02	0.00	0.00	5.90
BI_2022_04kN	4	Cylindrical (flat)	Avg	4.06	9.02	0.30	1169.08
			SD	0.02	0.00	0.00	0.76
BI_2022_06kN	6	Cylindrical (flat)	Avg	3.85	9.02	0.30	1235.23
			SD	0.03	0.00	0.00	2.53
BI_2022_09kN	9	Cylindrical (flat)	Avg	3.68	9.02	0.30	1291.25
			SD	0.02	0.00	0.00	5.90
BI_2022_12kN	12	Cylindrical (flat)	Avg	3.61	9.03	0.30	1315.78
			SD	0.02	0.00	0.00	5.85
BI_2022_15kN	15	Cylindrical (flat)	Avg	3.56	9.02	0.31	1340.70
			SD	0.02	0.00	0.00	8.72

a linear modifying function cancels out in Eq. 10. As a result, the original K-K form is satisfied in the entire frequency range.

Micro-scale Dissipation Models for Viscoelastic Materials

As a linear energy dissipation mechanism, granular-level material visco-elasticity, internal friction, and inter-granular visco-elastic coupling in a granular matter are often modeled with visco-elastic continuum material models, in which both stress and strain relaxations are taken into consideration simultaneously. In the current work, the following

one-dimensional linear equation of motion in stress (σ_{xx}) and strain (ε_{xx}) with the generalized first-order visco-elastic material model with $m = n = 1$ is employed:

$$\sigma_{xx} + \sum_{i=1}^{n} p_i \frac{\partial^i \sigma_{xx}}{\partial t^i} = E\left(\varepsilon_{xx} + \sum_{i=1}^{m} q_i \frac{\partial^i \varepsilon_{xx}}{\partial t^i}\right)$$
$$\Rightarrow \sigma_{xx} + p_1 \frac{\partial \sigma_{xx}}{\partial t} = E\left(\varepsilon_{xx} + q_1 \frac{\partial \varepsilon_{xx}}{\partial t}\right) \tag{12}$$

where E is the elastic modulus, and p_1, q_1 the stress and strain relaxation times, respectively, which are rate-dependent material constants, as discussed in [43]. With Eq. 12 and the equation of longitudinal motion, $\rho \partial^2 u/\partial t^2 = \partial \sigma_{xx}/\partial x$, with

Table II Time-of-Flight (ToF_L and ToF_T) for Pressure and Shear Waves, Pressure, and Shear Wave Speeds (c_L and c_T), the Ratio of the Pressure and Shear Speed (κ), the Corresponding Young's Moduli (E_A), Shear Moduli (G_A), Poisson's Ratio (ν), Corrected Stress Relaxation Time (p_1^{cor}), Corrected Strain Relaxation Time (q_1^{cor}), and Scat- tering Constant (A) Are Listed with their Averages and SDs for the Six Levels of Compaction Force F_c of the Complete BI_2022 Sample Set. Each Sample Sub-set in the Complete BI_2022 Sample Set Consists of Four Tablets. The Total Number of Tablets in the Complete BI_2022 Sample Set Is Twenty-Four

| Sample set		Measured and extracted parameters										
		ToF_L	ToF_T	c_L	c_T	κ	E_A	G_A	ν	ϕ^m (%)	p_1^{cor}	q_1^{cor}	A
		(µsec)	(µsec)	(m/sec)	(m/sec)	(c_L/c_T)	(GPa)	(GPa)			(µsec)	(µsec)	($\times 10^{-27}$ (s/m)^4)
BI_2022_02kN	Avg	4.25	6.68	1086.32	691.65	1.57	1.21	0.49	0.16	29.33	0.05	0.13	N/A
	SD	0.09	0.38	28.64	43.97	0.07	0.06	0.06	0.06	0.33	0.07	0.02	N/A
BI_2022_04kN	Avg	2.82	4.56	1443.46	891.40	1.62	2.44	0.93	0.19	19.15	0.14	0.40	⁻15.50
	SD	0.08	0.02	37.85	3.43	0.05	0.12	0.01	0.03	0.05	0.02	0.03	4.29
BI_2022_06kN	Avg	2.32	3.75	1663.05	1027.59	1.62	3.42	1.31	0.19	14.58	0.16	0.41	− 6.53
	SD	0.01	0.10	19.69	27.83	0.04	0.07	0.07	0.03	0.18	0.02	0.04	2.44
BI_2022_09kN	Avg	2.08	3.15	1773.25	1169.00	1.52	4.06	1.76	0.10	10.70	0.17	0.50	− 7.07
	SD	0.03	0.04	28.26	15.94	0.02	0.12	0.04	0.01	0.41	0.03	0.04	2.79
BI_2022_12kN	Avg	1.98	2.90	1822.86	1246.73	1.46	4.37	2.05	0.08	9.02	0.22	0.66	− 9.07
	SD	0.06	0.05	47.09	16.44	0.03	0.22	0.05	0.03	0.39	0.03	0.10	0.28
BI_2022_15kN	Avg	1.82	2.82	1957.45	1265.19	1.55	5.14	2.15	0.14	7.28	0.23	0.72	− 9.74
	SD	0.04	0.01	41.59	7.20	0.03	0.22	0.01	0.03	0.60	0.03	0.12	1.76
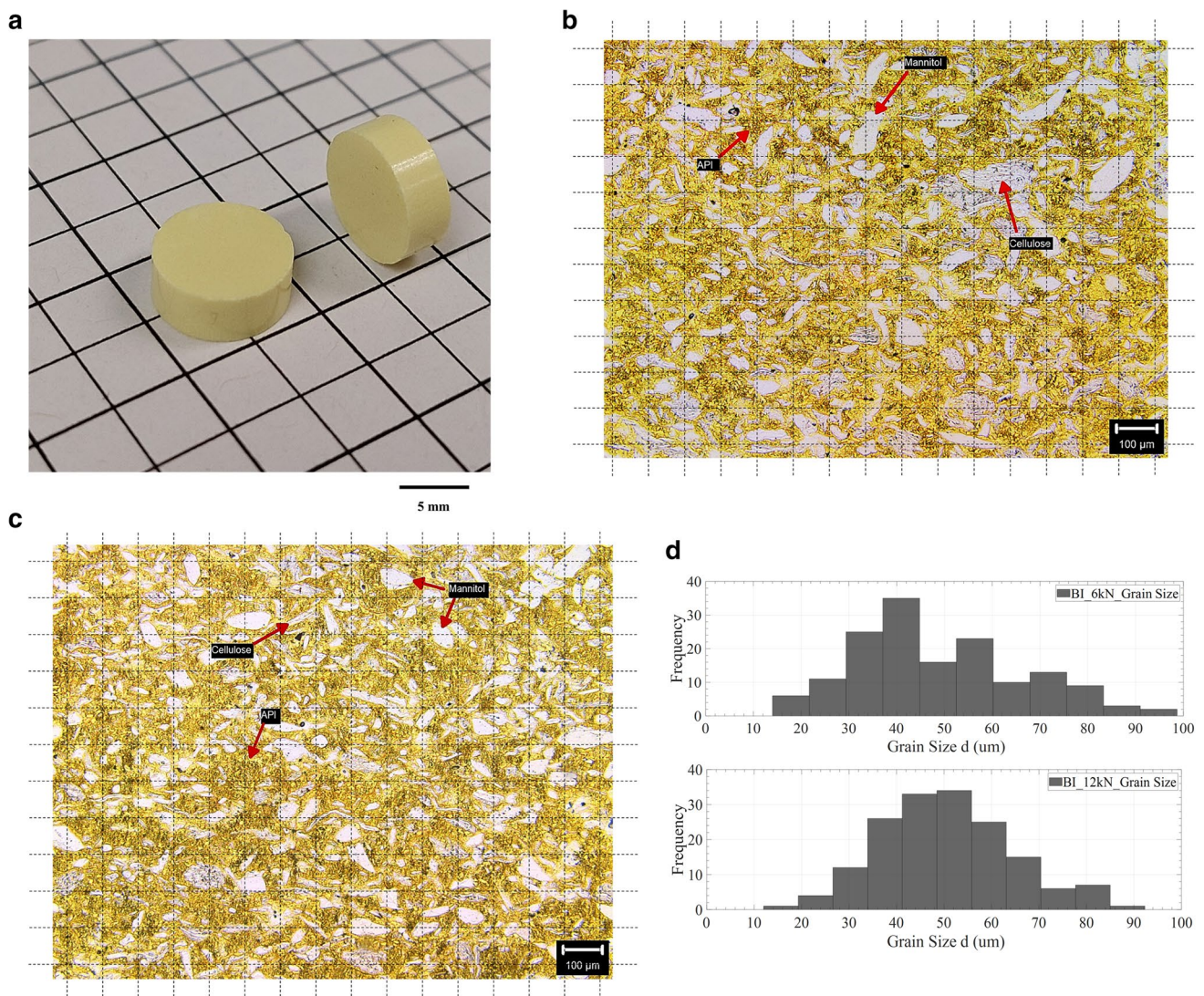
Fig. 1 Image of a sample from the BI_2022_15kN sub-set (**a**) (background grid: 5 mm×5 mm), the micro-structural images of two samples from the BI_2022_6kN and BI_2022_12kN sub-sets (**b**, **c**), and their article size distribution histograms (**d**)

$\varepsilon_{xx} = \partial u / \partial x$, where $u(x, t)$ and ρ are the traveling displacement field and the mass density, respectively, the wave equation for this first-order material model ($n=m=1$) is obtained as:

$$\frac{\partial^2 u}{\partial t^2} + p_1 \frac{\partial^3 u}{\partial t^3} = \frac{E}{\rho} \left(\frac{\partial^2 u}{\partial x^2} + q_1 \frac{\partial^3 u}{\partial x^2 \partial t} \right) \tag{13}$$

The visco-elastic attenuation and the corresponding dispersion relation are obtained using the dispersive displacement field $u(x, t) = U(\omega) e^{i(\kappa_v(\omega)x - \omega t)}$ with $\kappa(\omega) = \beta(\omega) + i\alpha(\omega)$ is the wavenumber, and $\alpha(\omega)$ and $\beta(\omega)$ are the attenuation and dispersion terms for the visco-elastic material, respectively. Here, setting $m=n=1$ in Eq. 12, a first-order visco-elastic standard linear solid (SLS) model is used for compressed OSD materials.

The standard linear solid (SLS), also referred to as the Zener visco-elastic material model, is a method of modeling the behavior of a visco-elastic material using a linear combination of springs and dashpots (dampers) to represent elastic and viscous components, respectively. The SLS model combines aspects of the Maxwell and Kelvin–Voigt models to more accurately describe the overall behavior of a material under a given set of dynamic loading conditions. The Maxwell model is unable to describe creep (or recovery) while the Kelvin–Voigt model includes no stress relaxation. The SLS model is the simplest model that includes both effects.

Procedure for Extracting Visco-elastic Parameters at Micro-scale

Mathematical Formulation

Assuming the propagation medium material is linearly visco-elastic (in the range of excitation displacement amplitudes) and stochastically granular, the experimentally obtained complex

wavenumber $\kappa(\omega) = \beta(\omega) + i\alpha(\omega)$ is modeled as linearly coupled (additively visco-elastic (v) and scattering (s)) effects. By plugging Eq. 5 into Eq. 13, and solving the resulting equation for $\alpha(\omega)$ with the symbolic computing system *Mathematica*™, the attenuation coefficient $\alpha(\omega; p_1, q_1)$ and real wavenumber $\beta(\omega; p_1, q_1)$ are expressed in closed-forms as four solution pairs as follows:

$$\left\{ \begin{array}{l} \alpha(\omega; p_1, q_1) = \mp\sqrt{\frac{D}{2}}, \beta(\omega; p_1, q_1) = \pm\sqrt{D}\,T \\ \alpha(\omega; p_1, q_1) = \mp\sqrt{\frac{Y}{2}}, \beta(\omega; p_1, q_1) = \pm\sqrt{Y}\,Q \end{array} \right\} \quad (14)$$

where

$$D \triangleq (c_L\omega)^2 \frac{-(1+p_1q_1\omega^2)(1+q_1^2\omega^2) - \sqrt{(1+p_1^2\omega^2)(1+q_1^2\omega^2)^3}}{c_L^4(1+q_1^2\omega^2)^2}$$

$$Y \triangleq (c_L\omega)^2 \frac{-(1+p_1q_1\omega^2)(1+q_1^2\omega^2) + \sqrt{(1+p_1^2\omega^2)(1+q_1^2\omega^2)^3}}{c_L^4(1+q_1^2\omega^2)^2}$$

$$T \triangleq (c_L\omega)^2 \frac{(1+p_1q_1\omega^2)(1+q_1^2\omega^2) - \sqrt{(1+p_1^2\omega^2)(1+q_1^2\omega^2)^3}}{\sqrt{2}(p_1-q_1)c_L^2\omega^3(1+q_1^2\omega^2)}$$

$$Q \triangleq (c_L\omega)^2 \frac{(1+p_1q_1\omega^2)(1+p_1^2\omega^2) + \sqrt{(1+p_1^2\omega^2)(1+q_1^2\omega^2)^3}}{\sqrt{2}(p_1-q_1)c_L^2\omega^3(1+q_1^2\omega^2)}$$

Below, by eliminating the common terms in Eq. 14, the attenuation coefficient $\alpha(\omega; p_1, q_1)$ and real wavenumber $\beta(\omega; p_1, q_1)$ are obtained in terms of each other (namely, the K-K relationships) for the *pure visco-elastic* (p_1, q_1) case (with the aid of *Mathematica*™):

$$\alpha(\omega; p_1, q_1) = \frac{(1+p_1q_1\omega^2) \pm \sqrt{(1+p_1^2\omega^2)(1+q_1^2\omega^2)}}{(p_1-q_1)\omega}\beta(\omega; p_1, q_1)$$

$$\beta(\omega; p_1, q_1) = -\frac{(1+p_1q_1\omega^2) \pm \sqrt{(1+p_1^2\omega^2)(1+q_1^2\omega^2)}}{(p_1-q_1)\omega}\alpha(\omega; p_1, q_1) \quad (15)$$

The experimentally extracted attenuation coefficient $\alpha^{exp}(\omega)$ and real wavenumber $\beta^{exp}(\omega)$ are represented for the complex wavenumber as two linearly-combined effects:

$$\alpha^{\exp}(\omega) = \alpha^v(p_1, q_1, \omega) + \alpha^s(d, \Delta d, \omega)$$
$$\beta^{\exp}(\omega) = \beta^v(p_1, q_1, \omega) + \beta^s(d, \Delta d, \omega) \quad (16)$$

where the superscripts v and s are for visco-elasticity and scattering, respectively, $d = \mu$ and $\Delta d = \sigma$ are the median scattered size and the standard deviation of its Gaussian distribution (or similar statistical parameters for an applicable probability distribution function). From Eq. 4, the experimentally obtained complex wavenumber $\kappa^{\exp}(\omega) = \beta^{\exp}(\omega) + i\alpha^{\exp}(\omega)$ from the two waveforms (Eq. 2) is determined as:

$$\kappa^{\exp}(\omega) + \beta^{\exp}(\omega) + i\alpha^{\exp}(\omega) = -i\frac{1}{h}\ln\left(\frac{F\{u(x=h,t)\}}{F\{u(x=0,t)\}}\right) \quad (17)$$

By substituting a harmonic solution in the form of $u(x,t) = Ae^{i(\kappa(\omega)x - \omega t)}$ into the visco-elastic wave equation

(Eq. 13), the complex wavenumber $\kappa(\omega)$ is expressed in terms of the visco-elastic parameters p_1 and q_1 as well as E and ρ. Expressing the visco-elastic parameters p_1 and q_1 in terms of the components of the complex wavenumber $\kappa^{\exp}(\omega)$ from Eq. (16) and substituting the experimentally obtained $\alpha^{exp}(\omega)$ and $\beta^{exp}(\omega)$ into those for the generalized visco-elastic model (Eq. 13), and by solving Eq. 15 for p_1 and q_1, the frequency-dependent values for $p_1^{\exp}$ and $q_1^{\exp}$ are obtained in closed form as follows:

$$p_1^{\exp}(\omega) = \frac{\left(\beta^{\exp}(\omega)^2 - \alpha^{\exp}(\omega)^2\right)\omega^2 - c_L\left(\beta^{\exp}(\omega)^2 + \alpha^{\exp}(\omega)^2\right)^2}{2\alpha^{\exp}(\omega)\beta^{\exp}(\omega)\omega^3}$$

$$\triangleq F_1(\alpha^{\exp}(\omega), \beta^{\exp}(\omega), \omega) \quad (18)$$

$$q_1^{\exp}(\omega) = \frac{c_L^2\left(\alpha^{\exp}(\omega)^2 - \beta^{\exp}(\omega)^2\right) + \omega^2}{2c_L^2\alpha^{\exp}(\omega)\beta^{\exp}(\omega)\omega} \triangleq F_2(\alpha^{\exp}(\omega), \beta^{\exp}(\omega), \omega)$$

The terms $p_1^{\exp}(\omega) \triangleq F_1(\alpha^{\exp}(\omega), \beta^{\exp}(\omega), \omega)$ and $q_1^{\exp}(\omega) \triangleq F_2(\alpha^{\exp}(\omega), \beta^{\exp}(\omega), \omega)$ functional forms in Eq. 18 are frequency dependent if the medium material is granular (with wave scatterers) as well as visco-elastic; thus, wave motion deviates from the *purely* visco-elastic dispersion behavior. If a linear medium is homogenous (e.g., not granular/textured) and *purely* visco-elastic, the corresponding terms $p_1^{\exp}(\omega)$ and $q_1^{\exp}(\omega)$ are expected to be constants (i.e., frequency-independent). Compressed OSD forms are often highly granular composites due to APIs and multiple excipients employed in their manufacturing. Propagating elastic waves in such granular media scatter in the Rayleigh regime if dominant wavelengths λ are considerably longer than d: $\lambda > 2\pi d$ with d is a characteristic grain diameter or pattern repetition length scale (periodicity) in Eq. 6.

For elastic wave propagation in the Rayleigh regime, with some real A and B parameter values, the following *corrected* approximation from Eq. 18 can be made for the *scatter-free* visco-elastic constants p_1 and q_1:

$$p_1^{cor}(\omega; A, B) \triangleq F_1(\alpha^{\exp}(\omega) - A\omega^4, \beta^{\exp}(\omega) - B\omega^4, \omega)$$
$$= \text{constant or near constant}$$
$$q_1^{cor}(\omega; A, B) \triangleq F_2(\alpha^{\exp}(\omega) - A\omega^4, \beta^{\exp}(\omega) - B\omega^4, \omega)$$
$$= \text{constant or near constant} \quad (19)$$
$$\alpha^{cor}(\omega; A) = \alpha^{\exp}(\omega) - A\omega^4$$
$$\beta^{cor}(\omega; B) = \beta^{\exp}(\omega) - B\omega^4$$

The experimentally obtained complex wavenumber is then represented in its pure visco-elastic and pure scattering components as:

$$\kappa^{\exp}(\omega) = \left(\beta^v(p_1^{cor}, q_1^{cor}, \omega) + \beta^s(d, \Delta d, \omega)\right)$$
$$+ i\left(\alpha^v(p_1^{cor}, q_1^{cor}, \omega) + \alpha^s(d, \Delta d, \omega)\right) \quad (20)$$

In other words, the extracted visco-elasticity coefficients $p_1^{\exp}(\omega)$ and $q_1^{\exp}(\omega)$ in Eq. 18 can be made frequency independent under ideal *Rayleigh* scattering conditions. This framework can be generalized for other scattering types (e.g., stochastic and transition and combined regimes) if the

presence of such scattering mechanisms is observed and/or anticipated from the texture of a medium.

Finally, once we verify that the propagation is in the *Rayleigh scattering* regime (with *visco-elasticity*), A^* and B^* can be further used to extract the grain/micro-structure properties of the medium (for example, the average grain size and its SD, and grain-to-grain elastic coupling) using the convolution integral method.

Extracting the Stress and Strain Relaxation Times p_1 and q_1 from the Experimental Dispersion Curves

The computational characterization task now requires the determination of the numerical values for the Rayleigh regime slopes A and B such that p_1^{cor} and q_1^{cor} are made constants (frequency-independent) or near constants. The first step is to determine a frequency interval (f_1, f_2) with $\omega = 2\pi f$ for which the delay-line response and sample responses will be non-zero. This selection should minimize numerical errors associated with zero division and/or loss of precision due to near-zero division. The frequency interval (f_1, f_2) is often within the transducer's bandwidth, as strong attenuation in the sample creates a cut-off frequency for transmitting high-frequency waves. A practical approach for choosing this interval would be to set an amplitude limit (for example, 5% of the maximum sample response in the frequency domain) for zero amplitude and determine the crossing points for this limit for which the *f*-coordinate would provide the frequency interval (f_1, f_2).

A numerical iteration solution by altering A and B until visually determining the values A and B is to make the curves $p_1^{cor}(\omega; A, B)$ and $q_1^{cor}(\omega; A, B)$ flat (or near-flat), indicating frequency independence. For the numerical iteration solution, ranges for the pairs (p_1 and q_1) and (A and B) are obtained from the direct simulations by exploring a range of values for A and B. Note that it is often observed that $p_1^{cor}(\omega)$ and $q_1^{cor}(\omega)$ are less sensitive to the parameter B (than they are to A), thus $B = 0$ is taken to simplify Eq. 19 into:

$$
\begin{aligned}
p_1^{cor} &= p_1^{cor}(\omega; A, 0) = F_1\left(\alpha^{\exp}(\omega) - A\omega^4, \beta^{\exp}(\omega), \omega\right) \\
&= \text{constant(or near} - \text{constant)} \\
q_1^{cor} &= q_1^{cor}(\omega; A, 0) = F_2\left(\alpha^{\exp}(\omega) - A\omega^4, \beta^{\exp}(\omega), \omega\right) \\
&= \text{constant (or near} - \text{constant)}
\end{aligned}
\tag{21}
$$

Finally, the $p_1^{cor}(\omega; A, 0)$ and $q_1^{cor}(\omega; A, 0)$ functions are plotted to verify if they are flat or near flat in (f_1, f_2).

Extracting the Mechanical Properties

Short-term Fourier Transform (STFT) time–frequency approaches are used to determine ToF_L and ToF_T from the acquired longitudinal and transverse waveforms, which

require the ToF of strain energy at a particular frequency [44]. The average longitudinal and pressure wave speeds (c_L and c_T) for a sample with thickness h are computed as follows:

$$
c_L = h/\text{ToF}_L \quad c_T = h/\text{ToF}_T
\tag{22}
$$

The apparent Young's modulus of the material is approximated by $E_A = c_L^2 \times \rho_A$, and for shear modulus is determined by $G_A = c_T^2 \times \rho_A$, where ρ_A is the apparent mass density of the sample material, assuming one-dimensional wave propagation. Assuming an isotropic material, the Poisson's ratio (ν) as a function of the wave speed ratio $\kappa = c_L / c_T$ is determined by:

$$
\nu(\kappa) = \frac{1}{2}\left(\frac{\kappa^2 - 2}{\kappa^2 - 1}\right)
\tag{23}
$$

The true densities (ρ_t) of the material were quantified on a helium displacement pycnometer (AccuPyc® 1340, Micromeretics, Norcross, Georgia, USA) using the method addressed in the United States Pharmacopeia (USP) < 699 > on the density of solids. After the material had been adjusted in a desiccator for more than 24 h, these measurements were carried out three times. Using the bulk (ρ_b) and true (ρ_t) densities of the compacts, the mass porosity (ϕ^m) of the sample compact in percentage (%) was calculated by:

$$
\phi^m(\%) = \left(1 - \frac{\rho_b}{\rho_t}\right) \times 100
\tag{24}
$$

Experimental Setup and Ultrasonic Waveform Acquisition

OSD Materials

In this work, the material matrix was a fluid bed granulation batch with a preclinical API (with weakly basic Biopharmaceutical Classification System (BCS)—II with the molecular weight (MW) $\approx$ 450 g/mol), mannitol, and microcrystalline cellulose (MCC) with the weight percentage ratios of 50.0:20.5:20.0, respectively. Croscarmellose sodium (4.0%) and magnesium stearate (1.5%) were also used as disintegrant and lubricant, respectively. Hypromellose (4.0%) was used as the tablet coating. The formulation was selected based on the high drug load to assess micro-structural properties influenced by different from standard excipients. Compacting the samples utilized in the current study (Fig. 1a) was conducted using this granulated blend with the following sizing data: the 10%, 50%, and 90% quantiles of the blend particle size distribution were 80 μm, 295 μm, and 543 μm, respectively. As it is observed in the optical sectioning images of the sample cross-sections (Fig. 1b, c),

the resulting actual grain size after compaction is however considerably smaller than these values for the starting blend.

Tablet Sample Set

The BI_2022 sample set utilized in the reported experiments consists of twenty-four samples prepared at six compaction force levels F_c from 2 to 15kN (referred to as the BI_2022_02kN, BI_2022_04kN, BI_2022_06kN, BI_2022_09kN, BI_2022_12kN, BI_2022_15kN subsets) with a 9-mm flat-face punch-die set. The shape of the samples is cylindrical (see Fig. 1a for an image of a BI_2022_15kN sample). In Fig. 1b and c, the micro-structure images (obtained by optical sectioning) of two samples from the BI_2022_6kN and BI_2022_12kN sub-sets are illustrated. Based on these images, the grain size distributions (d^*) of the BI_2022_6kN and BI_2022_12kN samples are obtained from 14 to 98 μm and from 12 to 92 μm, respectively (Fig. 1d). The average dimensions and mass densities of the BI_2022 samples are reported in Table I. The apparent mass density ($\rho_A = m_A/V$) of the tablet samples was determined using a CD-6 Absolute Digimatic Caliper (Mitutoyo Inc., Aurora, Illinois, USA) and a digital scale (Model: A120S-L, Mettler-Toledo Inc., Columbus, Ohio, USA) and are also reported in Table I.

Ultrasonic Experimental Setup and Equipment

To improve the accuracy and repeatability of non-destructive ultrasonic measurement, a robotic tablet handling system (TOTO, Pharmacoustics Technologies, LLC, Potsdam, New York, USA) was developed and utilized. In the development of the TOTO setup, a collaborative robot (UR3e, Universal Robots, Odense S, Denmark), ROBOTIQ HAND-E Adaptive Gripper (ROBOTIQ, Chemin Olivier, Lévis, Quebec, Canada), BOA spot vision system (BVS-SP-0640 M-XL-M08_w, Teledyne Imaging Sensors, Camarillo, California, USA), Standard Output Backlight (SOBL) platform (A-SV-SOBL-150×150-WHI, Smart vision light, Norton Shores, Michigan, USA), two pressure transducers (V540-SM, Olympus Corporation, Center Valley, Pennsylvania, USA) with a central frequency of 2.25 MHz, two shear wave transducers (V154-RM, Olympus Corporation, Center Valley, Pennsylvania, USA) with a central frequency of 1 MHz, and a pair of Rexolite™ delay-lines have been integrated. A LabVIEW (Version 2015, National Instruments Corp., Austin, Texas, USA)-based graphical user interface (GUI) controlling both the Ultrasonic Measurement Instrument (UMI 2022) (Pharmacoustics Technologies, LLC, Potsdam, New York, USA) and the TOTO robotic system was developed and utilized for data acquisition and processing for this study (Fig. 2).

The current automated experimental setup is designed for acquiring pressure and shear waves in both pitch-catch (PCM) and pulse-echo modes (PEM) to characterize the physical, mechanical, and visco-elastic properties of pharmaceutical OSDs in a repeatable manner. In the reported experiments, the setup in PCM was set to a pulse width of 200 ns, a pulser voltage of 300 V, a sampling rate of 100 MHz, an amplification gain of 0 dB, and an averaged (oversampling) rate of 512. The data acquisition procedure is similar to the TOTO robotic handling system utilized in [14].

Ultrasonic Waveform Acquisition and Signal Processing

In the reported experiments, both pressure and shear responses of the OSD samples are acquired in PCM. For the calibration waveform acquisition, the pulser-out transducer mounted with the delay-line is put in contact with the receiving transducer by the TOTO system, and an ultrasonic wave pulse is transmitted through the delay-line and received by the receiving transducer. The acquired calibration waveform forms a baseline for determining the time-of-flight information for samples. For the ultrasonic response acquisition for the samples, the positional and geometric information (e.g., position, orientation, major, and minor axis length) of the OSD is determined using the spot BOA vision system of the TOTO system by acquiring the sample image placed on the SOBL backlight source. Using this position and geometric information of the OSD, the collaborative robot grips the OSD from the backlight source and places it on the testing platform (on top of the receiving transducer surface) (Fig. 2a). Afterward, the pulser pressure transducer mounted with the delay-line is positioned in the axial direction of the OSD by the collaborative robot and exerts a constant axial load of 25 N on the sample to ensure reliable wave transmission while acquiring sample response waveforms. Using the GUI of the UMI 2022 equipment, the time-of-flight (ToF_L, ToF_T), the pressure and share wave speeds of the propagating wave pulses (c_L, c_T), the visco-elastic parameters (p_1, q_1), and scattering constant (A) are obtained from the calibration waveform and the sample response of the OSD. Finally, the collaborative robot returns the tested OSD to a storage container. This process of unsupervised data acquisition continues until the last sample is processed. The same procedure is repeated to acquire transverse (shear) waveform data of the same sample set with the shear transducer pair.

Results and Discussions

The mathematical and experiment frameworks presented in the current study are based on the effect of visco-elasticity and wave scattering due to internal microstructures due to frequency-dependent attenuation of ultrasonic pressure and
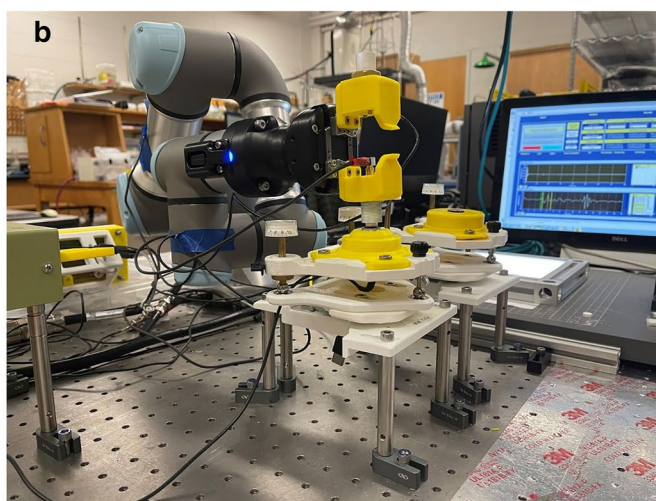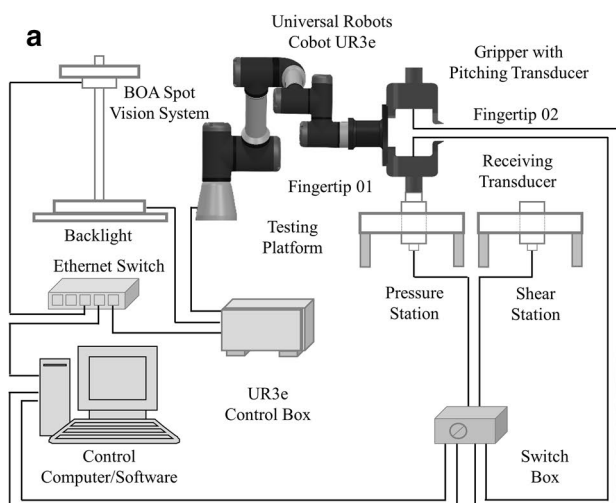
a

b

Fig. 2 a Connectivity diagram of the experimental rig (TOTO experimental setup) consisting of a BOA Spot vision system for locating the sample position, a collaborative robot as the sample handling system, a cobot gripper integrated with the pulsing shear transducers for sample picking and ultrasonic testing, and the receiving pressure and shear transducer holders for operating the system in the pitch-catch mode. **b** Image of the TOTO experimental setup

shear pulses propagating in a granular tablet medium. Pressure (P) and shear (S) waveforms acquired in pitch-catch mode (PCM) with the experimental setup, corresponding pressure, and shear waveforms, with amplitude normalization, are depicted in Fig. 3a and b. To determine the visco-elasticity and scattering coefficients, the longitudinal waveforms acquired from pitch-catch mode were transformed into the spectral domain using a fast Fourier transform (FFT) routine (Fig. 4a, b). From experimentally acquired pressure waveforms, the attenuation coefficient $\alpha(\omega)$ and real wavenumber $\beta(\omega)$ were calculated based on Eq. (4), by comparing the two waveforms in the corresponding frequency interval (f_1, f_2) in the transducer bandwidth.

In Fig. 4c and d, the comparisons of the experimental and corrected attenuation coefficients ($a(f)$ and $a^{cor}(f)$), and (real) wavenumber ($\beta(f)$ and $\beta^{cor}(f)$) as a function of frequency (f) were shown in the transducer bandwidth (0.8–2.6 MHz) for the BI_2022_09kN sub-set, where the corrected attenuation coefficient $a^{cor}(f)$ and the corrected (real) wavenumber $\beta^{cor}(f)$ present the prescribed values of the attenuation and real wavenumber of the dispersion curve for the extracted material property (namely $c_L = 1790.12$ m/s, $p_1 = 0.1459$ μs, $q_1 = 0.4470$ μs). For the dispersion curve calculation, only the visco-elastic effect is considered with no scattering effect, which is called the un-modeled scattering component. It is observed that the (real) wavenumber $\beta(f)$ and the corrected (real) wavenumber $\beta^{cor}(f)$ curves are in relatively close agreement (Fig. 4d), which is supporting the proposed approach. Theoretically, $\beta(f) = \beta^{cor}(f) + B \omega^4$ (Eq. 19), where scattering constant $B = 0$ is taken (Eq. 21). The attenuation coefficient $a(f)$ and the corrected attenuation coefficient $a^{cor}(f)$ curves slightly deviate in the transducer bandwidth. The deviations

observed in the attenuation coefficients (Fig. 4c) could be attributed to the un-modeled scattering contribution to the dispersion curve, which also supports the proposed mathematical formulation, because, by the theory, the attenuation term is in the form of $a(f) = a^{cor}(f) + A \omega^4$, where A is the scattering constant (Eq. 19). The similar trend of the experimental and corrected attenuation coefficients ($a(f)$ and $a^{cor}(f)$), and (real) wavenumber ($\beta(f)$ and $\beta^{cor}(f)$) is observed for the BI_2022 samples pressed at other compaction forces. This observation supports the existence of strong scattering in the experimentally acquired waveforms.

In Fig. 5, the extracted and corrected visco-elastic material properties (stress (p_1 and p_1^{cor}) and strain (q_1 and q_1^{cor}) relaxation times (log scale)) from the experimental waveform for the BI_2022 sub-sets are shown as a function of frequency in the transducer bandwidth. It is demonstrated that in Fig. 5 (left) the experimentally extracted $p_1(\omega)$ and $q_1(\omega)$ curves are in a decreasing trend in the frequency range of 0.8–2.6 MHz, whereas the corrected p_1^{cor} and q_1^{cor} curves are nearly flat (Fig. 5, right). To eliminate the deviations between the extracted and corrected p_1^{cor} and q_1^{cor} curves, scattering constants (A and B) are introduced to evaluate the scattering effect on the experimentally extracted frequency dependency $p_1(\omega)$ and $q_1(\omega)$ curves. The contributions of the scattering constants (A and B) on the extracted $p_1(\omega)$ and $q_1(\omega)$ curves compared to the corrected p_1^{cor} and q_1^{cor} curves in the transducer bandwidth are shown in Fig. 5 (right). It is observed that the extracted $p_1(\omega)$ and $q_1(\omega)$ curves become nearly flat in the frequency range of 0.8–2.6 MHz by varying the scattering constants (A and B) (Fig. 5 (right)).

The parameters ρ_A, c_L, c_T, E_A, G_A, and ν as functions of the compaction force F_c for the BI_2022 sub-sets are presented in Fig. 6a-c. It is observed that the ρ_A, c_L, c_T, E_A,
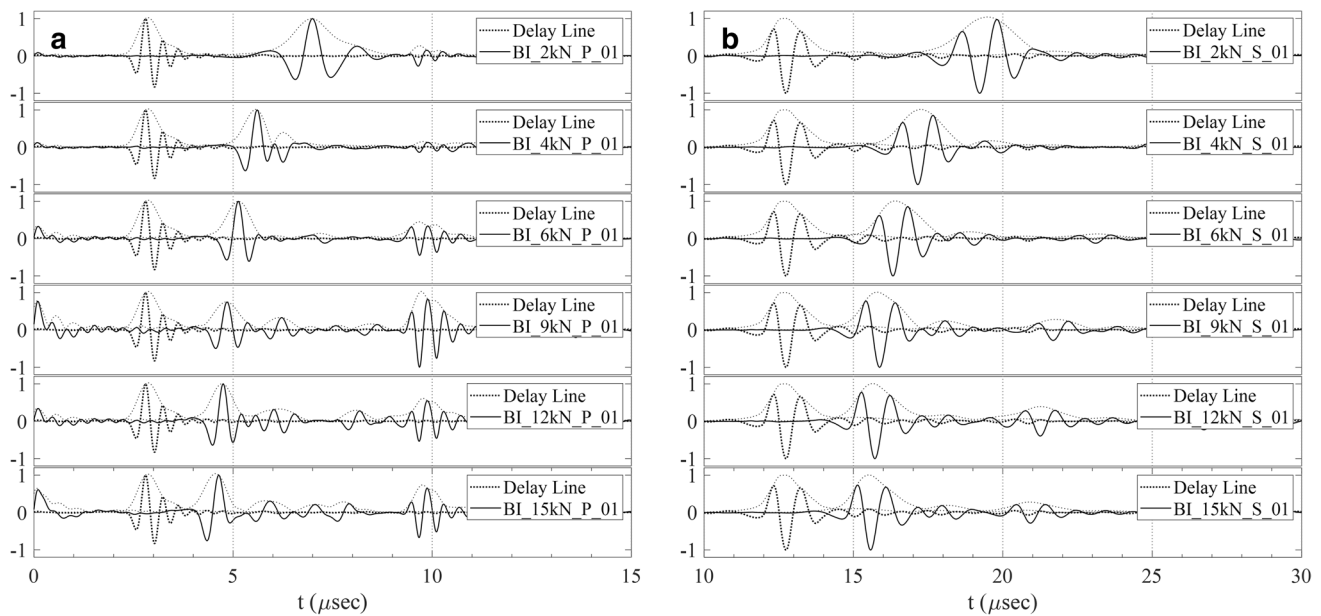
Fig. 3 Normalized pressure (**a**) and shear (**b**) waveforms for the complete BI_2022 sample sets with the delay-line waveform (dotted) at the corresponding compaction forces. Light-dotted lines represent the Hilbert transform of the waveform

and G_A curves for all sample sets increase with increasing compaction force F_c, indicating the pressure and shear wave speeds (c_L and c_T) were strongly modulated by F_c. With increasing F_c, it is reported that the values of Poisson's ratio ν for compacts often decrease [14]. In the reported study, for the BI_2022 sample set with $F_c = 4$, 6, 9, and 12 kN, it is indeed observed that ν decreases with increasing F_c (Fig. 6c). However, for $F_c = 2$ kN and $F_c = 15$ kN, a reverse trend is observed. It is known that low speed ratio values $\kappa = c_L/c_T$ result in high errors in ν predictions for compacts [15]. As reported in Table II, the range of κ is approximately from 1.4 to 1.6, which is considered low, so considerable errors in ν predictions are expected. For $F_c = 2$ kN, the SD (standard deviation) of $\kappa = 0.07$ (with SD (%) = 4.46%) and for $F_c = 15$ kN, the SD of $\kappa = 0.03$ (with SD (%) = 1.94%) (Table II) are obtained, leading to high error levels in ν predictions (for $F_c = 2$ kN and 15 kN the SD (%) of ν is 37.5% and 21.43%, respectively) and an unexpected reverse trend in the ν-F_c relation (Fig. 6c). By using advanced time–frequency signal processing techniques, the accuracy of ν determination could be improved, as such techniques should result in less errors in the speeds-of-sound measurements (c_L, c_T), which is the known source of the error in the ν determination [15].

In Fig. 6d, the effect of the tablet compaction force F_c on the corrected stress (p_1^{cor}) and strain (q_1^{cor}) relaxation time in the samples is demonstrated and quantified. For the complete BI_2022 sample set, the corrected stress relaxation time (p_1^{cor}) and strain relaxation time (q_1^{cor}) increase with the compaction force F_c using different scattering constants (A and B). According to Eq. 21, $p_1^{cor}(\omega)$

and $q_1^{cor}(\omega)$ are significantly less sensitive to the scattering constant B; thus, $B = 0$ is taken without loss of precision. The frequency bandwidth of BI_2022_2kN is in the range of 0.5 to 1.8 MHz (Fig. 4b). For the BI_2022_02kN sample material (Table II), $c_L = 1086.32$ m/s, when it is excited at the upper bound of its frequency band, namely at $f_{upper} = 1.8$ MHz, the shortest wavelength of the pressure wave pulse is approximated as $c_L/f = \lambda = 603.34$ μm (Eq. 6). Thus $\lambda \sim 2\pi\, d^*$, leading to a crossover grain diameter of $d^* = 96.02$ μm from Rayleigh regime to stochastic regime. From the microstructural image of the BI_2022_06kN and BI_2022_12kN (Fig. 1b, c), it is observed that the vast majority of grains in the composites are smaller than the crossover grain diameter $d^* = 96.02$ μm, therefore scattering experienced in the reported experiments occurs predominantly in the Rayleigh regime. In contrast, p_1^{cor} and q_1^{cor} values decreased with increasing porosity ϕ^m (%) (Fig. 7). Both corrected stress (p_1^{cor}) and strain (q_1^{cor}) relaxation times are strongly modulated by the compaction force F_c and porosity ϕ^m (%). The complete set of the measured and calculated physical, mechanical, and viscoelastic properties is reported in Table II.

Conclusions and Remarks

Typically, advanced compressed (OSD) tablet forms are strongly visco-elastic and highly granular, thus a characterization approach must be capable of dealing with both effects simultaneously in the relevant temporal, spatial, and spectral

Fig. 4 a Spectral responses of the complete BI_2022 sample sets with the delay-line (dotted) for longitudinal (pressure) waveform (**b**) spectral responses of the BI_2022_09kN sample set with the delay-line (dotted) for longitudinal (pressure) waveform with the transducer bandwidth (0.8–2.6 MHz). Comparisons of the experimental and corrected extracted (**c**) attenuation coefficient (α(f) and α^{cor}(f)), **d** (real) wavenumber (β(f) and $\beta.^{cor}$(f)) as a function of frequency within the transducer bandwidth (0.8–2.6 MHz)
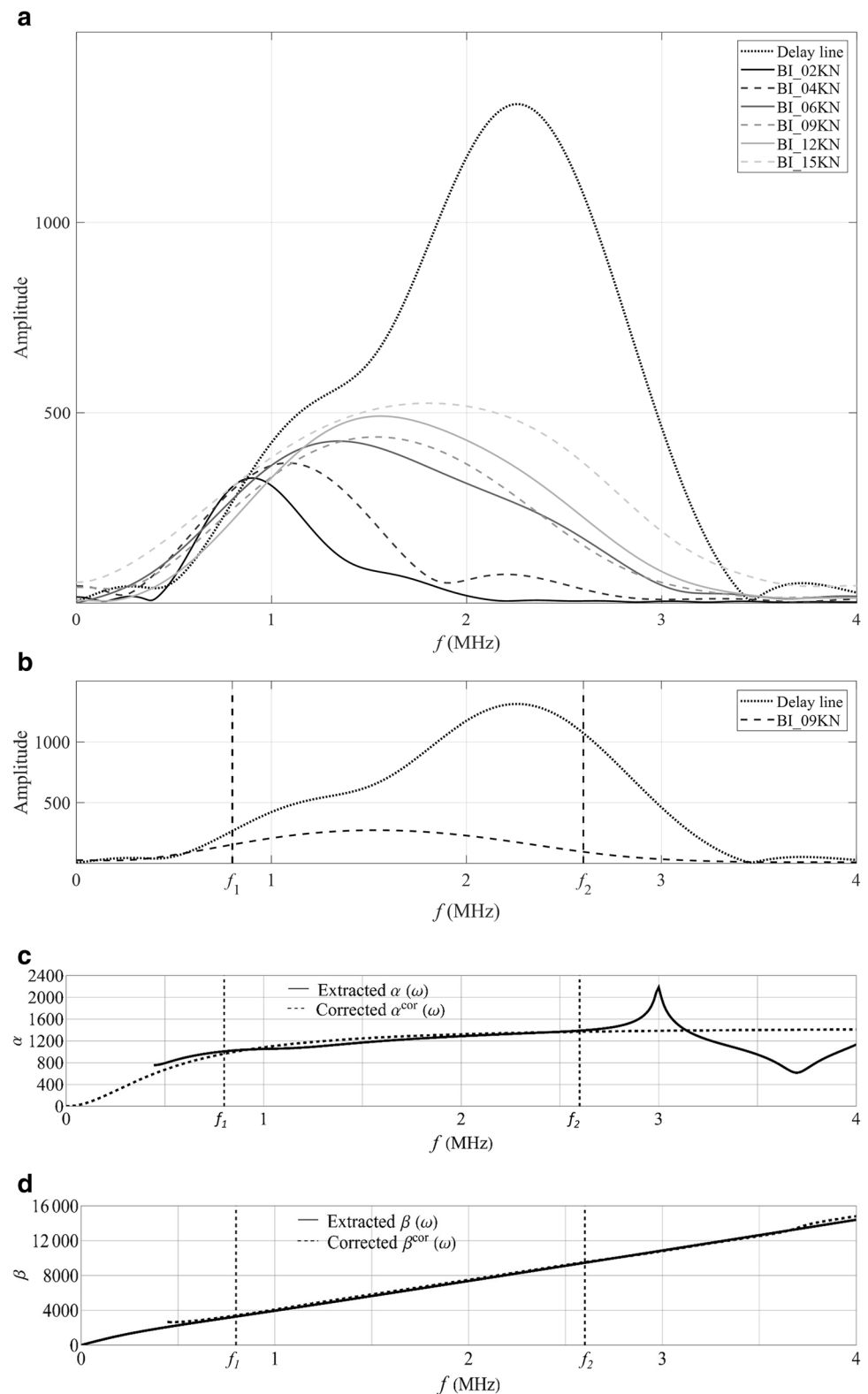
scales. In the current work, a deterministic non-destructive ultrasonic technique and an associated mathematical formulation for extracting the visco-elastic material properties and scattering parameters of granular OSD materials simultaneously from their experimentally obtained attenuation characteristics are presented and demonstrated for the first time. Using the two-parameter Zener model, a set of visco-elastic and scattering material parameters, including stress

Fig. 5 Comparisons of the experimental extracted and corrected stress ($p_{1(\omega)}$ (left column) and p_1^{cor} (right column)) and strain ($q_{1(\omega)}$ (left column) and q_1^{cor} (right column)) relaxation time in log scale as a function of frequency within the transducer bandwidth (0.8–2.6 MHz) for the complete BI_2022 sample sets. The gray lines are for p_1 and p_1^{cor} and the dark solid lines are for q_1 and q_1^{cor}
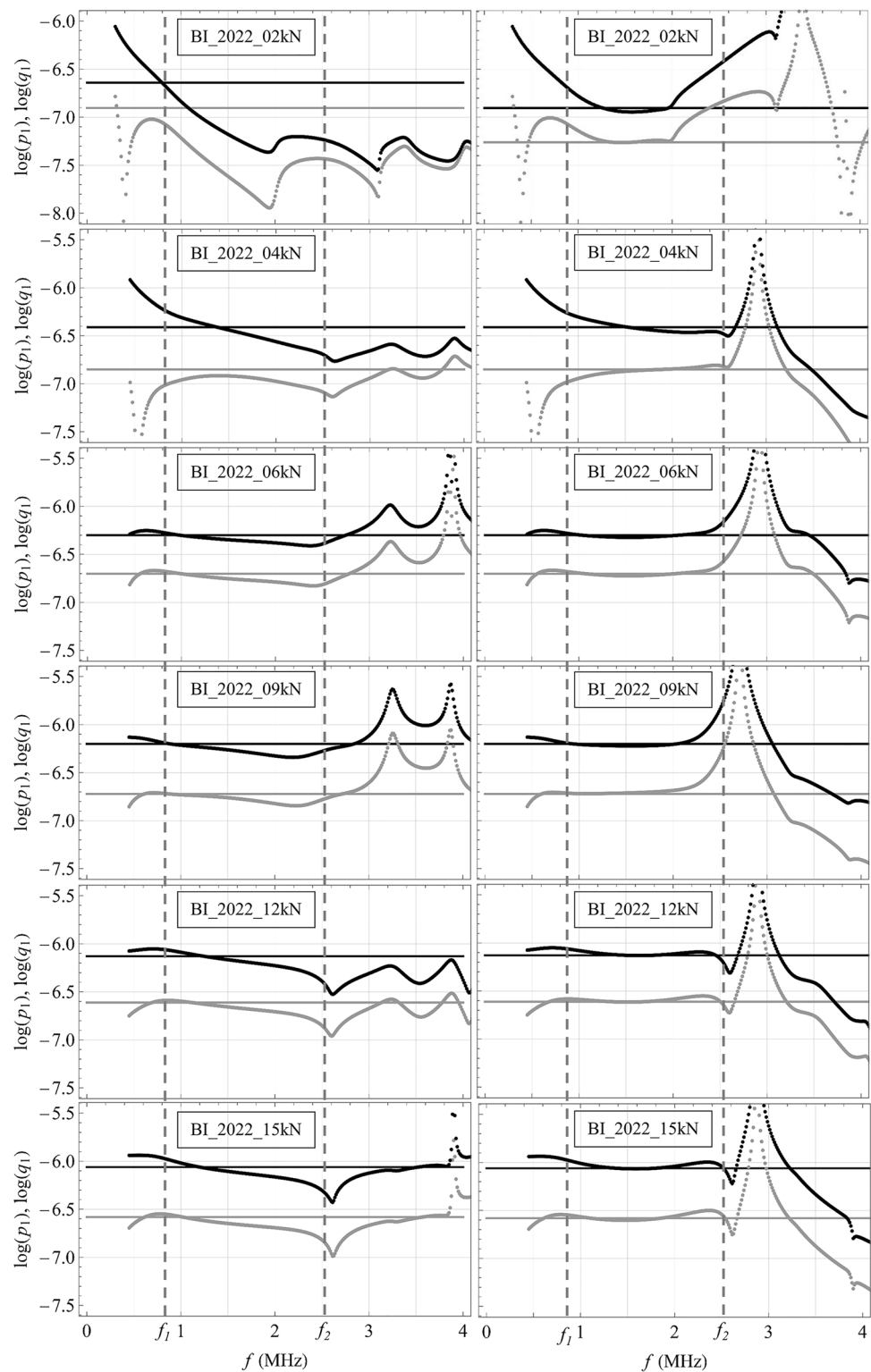
relaxation time (p_1), strain relaxation time (q_1), and scattering constants (A and B) were extracted along with the macromechanical properties including the mean Young's (E_A), shear moduli (G_A), and Poisson's ratio (ν). The contributions of visco-elastic and scattering attenuation are determined and

compared by applying the extracted material parameters to the linear visco-elastic attenuation and Rayleigh scattering attenuation models, respectively. It is observed that the stress relaxation (p_1^{cor}) and strain relaxation (q_1^{cor}) times of the compact increase with increasing compaction force (F_c). The observed

Fig. 6 Relationship between the compaction force F_c and **a** pressure wave speeds (c_L) and shear wave speeds (c_T), **b** apparent Young's (E_A) and shear (G_A) moduli, **c** apparent densities (ρ_A) and Poisson's ratio (ν), **d** p_1^{cor} and q_1^{cor}, and **e** $A \times 10^{-27}$ (s/m)^4 value for the complete BI_2022 sample sets
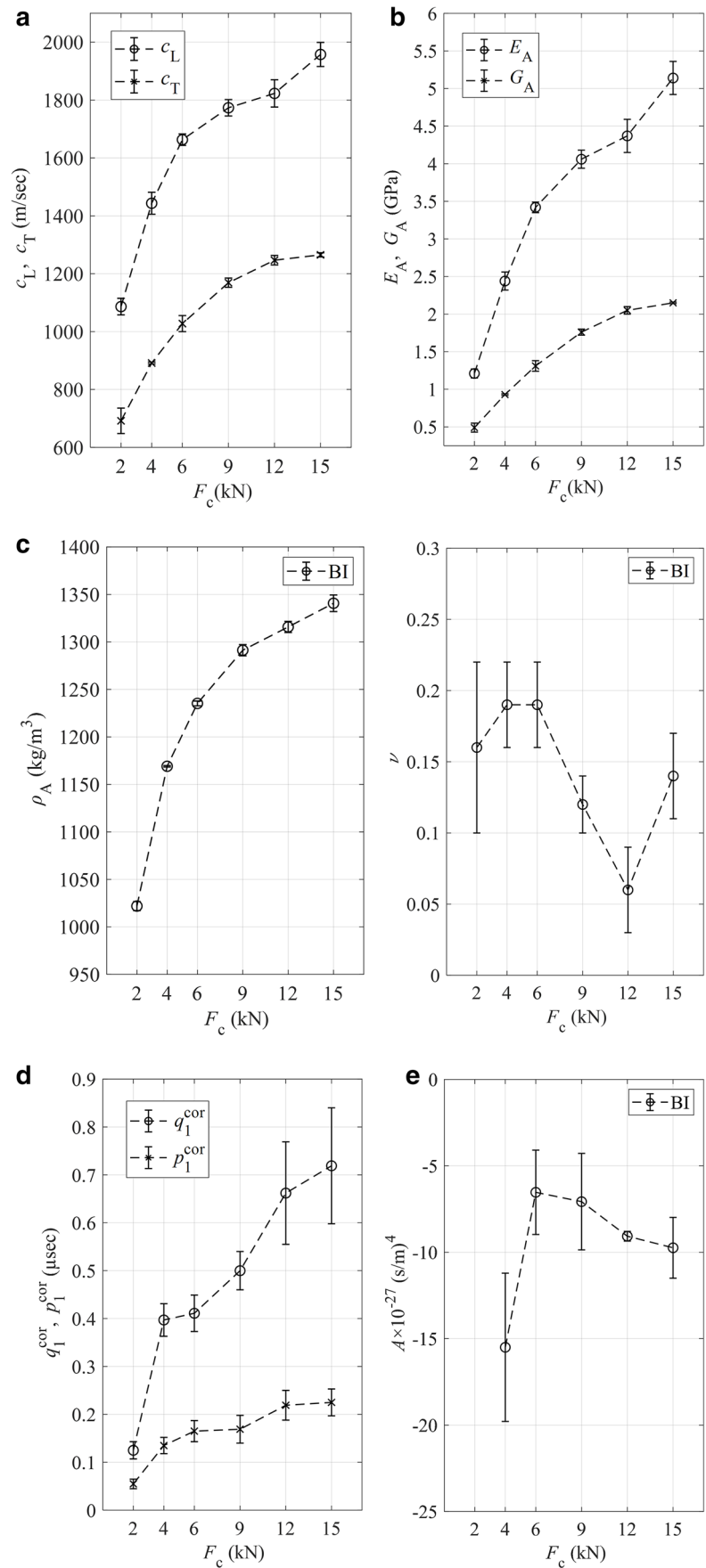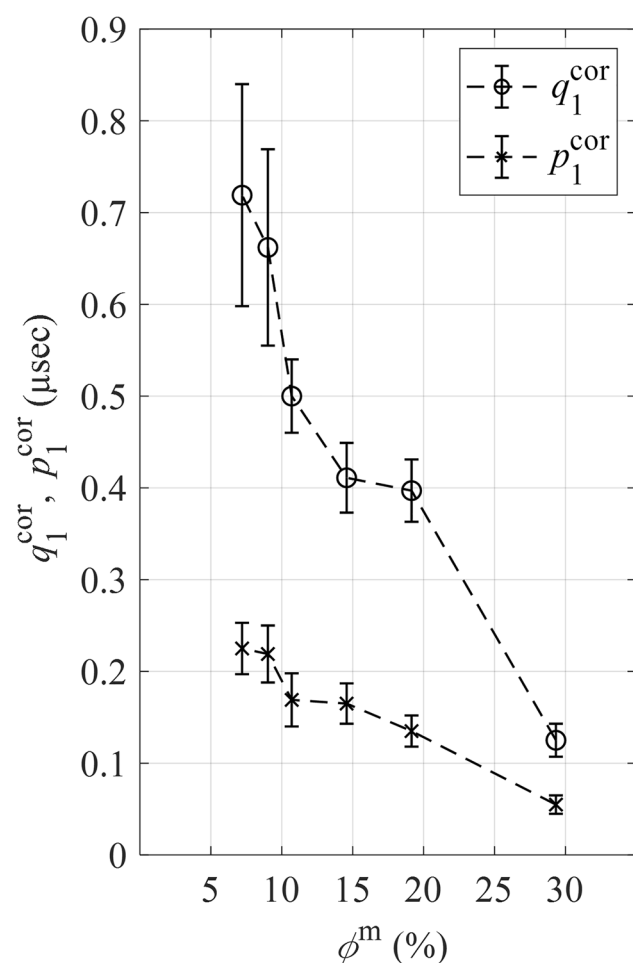
Fig. 7 The relationships between the directly measured ϕ^m (%) and acoustically extracted p_1^{cor} and q_1^{cor} for the complete BI_2022 sample sets

trend of increasing p_1^{cor}, and q_1^{cor} as a function of compaction force (F_c) is as expected.

At present, in the pharmaceutical manufacturing industry, a strong need for conducting on-site rapid real-time release (RTR) tests during manufacturing in a non-destructive manner is emerging. The presented automated experimental approach incorporating the proposed algorithmic characterization framework for extracting the micro-visco-elastic parameters along with the mechanical and physical properties of compacts could play a key role in developing non-destructive ultrasonic techniques to address this practical need. Consequently, the ultrasonically extracted micro-visco-elastic properties of a tablet product could be linked to its critical quality attributes (CQAs) in a rapid, non-destructive manner. For real-time *in situ* monitoring of the micro-visco-elastic properties, machine learning (ML) models can also be trained with synthetic and experimentally extracted waveforms using the proposed novel mathematical framework. With a trained ML model, RTR testing time and cost could significantly be reduced with an increased quality assurance level.

Declarations

Conflict of Interest The authors disclose no competing interests.

References

1. Saravanan M, Nataraj KS, Ganesh KS. The Effect of tablet formulation and hardness on in vitro release of cephalexin from Eudragit L100 Based extended release tablets. Biol Pharm Bull. 2002;25(4):541–5.
2. Sun CC. Microstructure of tablet—pharmaceutical significance, assessment, and engineering. Pharm Res. 2017;34(5):918–28.
3. Braun RJ, Parrott EL. Influence of viscosity and solubilization on dissolution rate. J Pharm Sci. 1972;61(2):175–8.
4. Lum SK, Duncan-Hewitt WC. Deformation kinetics analysis of polymeric matrices. Pharm Res. 1996;13(5):692–700.
5. Hakulinen MA, Pajander J, Leskinen J, Ketolainen J, van Veen B, Niinimäki K, et al. Ultrasound transmission technique as a potential tool for physical evaluation of monolithic matrix tablets. AAPS PharmSciTech. 2008;9(1):267–73.
6. Serris E, Perier-Camby L, Thomas G, Desfontaines M, Fantozzi G. Acoustic emission of pharmaceutical powders during compaction. Powder Technol. 2002;128(2):296–9.
7. Ketolainen J, Oksanen M, Rantala J, Stor-Pellinen J, Luukkala M, Paronen P. Photoacoustic evaluation of elasticity and integrity of pharmaceutical tablets. Int J Pharm. 1995;125(1):45–53.
8. Varghese I, Cetinkaya C. Noncontact Photo-acoustic defect detection in drug tablets. J Pharm Sci. 2007;96(8):2125–33.
9. Akseli I, Cetinkaya C. Acoustic testing and characterization techniques for pharmaceutical solid dosage forms. J Pharm Innov. 2008;3(4):216–26.
10. Akseli I, Becker DC, Cetinkaya C. Ultrasonic determination of Young's moduli of the coat and core materials of a drug tablet. Int J Pharm. 2009;370(1):17–25.
11. Leskinen JT, Simonaho SP, Hakulinen M, Ketolainen J. In-line ultrasound measurement system for detecting tablet integrity. Int J Pharm. 2010;400(1):104–13.
12. Simonaho SP, Takala TA, Kuosmanen M, Ketolainen J. Ultrasound transmission measurements for tensile strength evaluation of tablets. Int J Pharm. 2011;409(1):104–10.
13. Akseli I, Dey D, Cetinkaya C. Mechanical Property characterization of bilayered tablets using nondestructive air-coupled acoustics. AAPS PharmSciTech. 2010;11(1):90–102.

14. Sultan T, Xu X, Hasan Rozin E, Sorjonen J, Ketolainen J, Wikström H, et al. Effect of shape on the physical properties of pharmaceutical tablets. Int J Pharm. 2022;25(624): 121993.

15. Sultan T, Paul S, Hasan Rozin E, Canino C, Tseng YC, Cetinkaya C. Ultrasonic characterization of complete anisotropic elasticity coefficients of compressed oral solid dosage forms. Int J Pharm. 2022;25(623): 121922.

16. Akseli I, Mani GN, Cetinkaya C. Non-destructive acoustic defect detection in drug tablets. Int J Pharm. 2008;360(1):65–76.

17. Paul S, Tseng YC. A semi-empirical model for estimation of flaw size in internally defective tablets. J Pharm Sci. 2021;110(6):2340–5.

18. Paul S, Baranwal Y, Tseng YC. An insight into predictive parameters of tablet capping by machine learning and multivariate tools. Int J Pharm. 2021;15(599): 120439.

19. Xu X, Vallabh CKP, Hoag SW, Dave VS, Cetinkaya C. Early detection of capping risk in pharmaceutical compacts. Int J Pharm. 2018;553(1–2):338–48.

20. Xu X, Mack C, Cleland ZJ, Vallabh CKP, Dave VS, Cetinkaya C. Correlation of solid dosage porosity and tensile strength with acoustically extracted mechanical properties. Int J Pharm. 2018;542(1–2):153–63.

21. Xu X, Coskunturk Y, Dave VS, Kuriyilel JV, Wright MF, Dave RH, et al. Effects of compaction pressure, speed and punch head profile on the ultrasonically-extracted physical properties of pharmaceutical compacts. Int J Pharm. 2020;15(575): 118993.

22. Meynard J, Amado-Becker F, Tchoreloff P, Mazel V. Characterization of the viscoelasticity of pharmaceutical tablets using impulse excitation technique. Int J Pharm. 2022;613: 121410.

23. Roney RK. The influence of metal grain structure on the attenuation of an ultrasonic acoustic wave [PhD Thesis]. California Institute of Technology; 1950.

24. Lücke K. Ultrasonic Attenuation caused by thermoelastic heat flow. J Appl Phys. 1956;27(12):1433–8.

25. Rippie EG, Danielson DW. Viscoelastic stress/strain behavior of pharmaceutical tablets: Analysis during unloading and postcompression periods. J Pharm Sci. 1981;70(5):476–82.

26. Stanke FE, Kino GS. A unified theory for elastic wave propagation in polycrystalline materials. The Journal of the Acoustical Society of America. 1984;75(3):665–81.

27. Karal FC Jr, Keller JB. Elastic, electromagnetic, and other waves in a random medium. J Math Phys. 1964;5(4):537–47.

28 Bhatia AB. Scattering of high-frequency sound waves in polycrystalline materials. J Acoust Soc Ame. 1959;31(1):16–23.

29. Hirsekorn S. The scattering of ultrasonic waves by polycrystals. The Journal of the Acoustical Society of America. 1982;72(3):1021–31.

30. Weaver RL. Diffusivity of ultrasound in polycrystals. J Mech Phys Solids. 1990;38(1):55–86.

31. Kube CM. Iterative solution to bulk wave propagation in polycrystalline materials. The Journal of the Acoustical Society of America. 2017;141(3):1804–11.

32. Turner JA. Elastic wave propagation and scattering in heterogeneous, anisotropic media: textured polycrystalline materials. 1999;13.

33. Yang L, Lobkis OI, Rokhlin SI. Shape effect of elongated grains on ultrasonic attenuation in polycrystalline materials. Ultrasonics. 2011;51(6):697–708.

34. Yang L, Lobkis OI, Rokhlin SI. Explicit model for ultrasonic attenuation in equiaxial hexagonal polycrystalline materials. Ultrasonics. 2011;51(3):303–9.

35. Smith CJ, Stephens JD, Hancock BC, Vahdat AS, Cetinkaya C. Acoustic assessment of mean grain size in pharmaceutical compacts. Int J Pharm. 2011;419(1):137–46.

36. SaeediVahdat A, Krishna Prasad Vallabh C, Hancock BC, Cetinkaya C. Ultrasonic approach for viscoelastic and microstructure characterization of granular pharmaceutical tablets. Int J Pharm. 2013;454(1):333–43.

37. Schmerr, Lester W. Fundamentals of ultrasonic nondestructive evaluation: a modeling approach [Internet]. 2nd ed. Springer International Publishing; 2016 [cited 2020 Oct 22]. (Springer Series in Measurement Science and Technology).

38. Morse PM. Vibration and sound. 2nd ed. McGraw-Hill; 1948. 468 p.

39. Papadakis EP. 15 - Ultrasonic Attenuation caused by scattering in polycrystalline media. In: Mason WP, editor. Physical Acoustics [Internet]. Academic Press; 1968 [cited 2020 Oct 23]. p. 269–328. (Applications to Quantum and Solid State Physics; vol. 4).

40. Merkulov LG. Investigation of ultrasonic scattering in metals. Sov J Technol Phys. 1956;26:59–69.

41. Smith RL. The effect of grain size distribution on the frequency dependence of the ultrasonic attenuation in polycrystalline materials. Ultrasonics. 1982;20(5):211–4.

42. Waters KR, Hoffmeister BK. Kramers-Kronig analysis of attenuation and dispersion in trabecular bone. The Journal of the Acoustical Society of America. 2005;118(6):3912–20.

43. Moe DV, Rippie EG. Nondestructive viscoelastic analysis of anisotropy in compressed tablets. J Pharm Sci. 1997;86(1):26–32.

44. Drai R, Khelil M, Benchaala A. Time frequency and wavelet transform applied to selected problems in ultrasonics NDE. NDT and E Int. 2002;35(8):567–72.